A Superconducting Permeameter for Characterizing Soft Magnetic Materials at High Fields

A Superconducting Permeameter for Characterizing Soft Magnetic Materials at High Fields

Pasquale Arpaia, Marco Buzio, Susana Izquierdo Bermudez, Annalisa Liccardo, Alessandro Parrella, Mariano Pentella, Pedro M. Ramos, and Edvard Stubberud

***Abstract*—A superconducting permeameter is proposed to characterize the magnetic properties of high-energy superconducting magnet yokes at their operating temperature and saturation level. The main problem of superconducting coils, an undesired quench, was faced by specific protection simulations, which has lead to a self-protected system. The superconducting permeameter was used to perform the magnetic characterization of ARMCO® Pure Iron, the material for the new High-Luminosity Large Hadron Collider (HL-LHC) superconducting magnet yokes, was performed at the cryogenic temperature of 4.2 K and a saturation level of nearly 3 T. Two case studies based on the new HL-LHC superconducting quadrupole and dipole magnets, highlight the impact of the magnetic properties of the yoke on the performance of the superconducting magnets, showing that the common assumption that heavily-saturated steels with similar chemical composition behave precisely the same way has been proved wrong.**

***Index Terms*—Magnetic measurement, superconducting magnets, hysteresis curves, permeameter, HL-LHC, magnet quench protection, magnetic materials, magnetic field quality**

I. Introduction

MAGNETIC fields are crucial elements in many basic applications of our society [1]–[3]. In electrical machines, the interaction between a magnetic field and a current creates a torque, thus mechanical power. In magnetic disk memories, the magnetic-field-induced changes in the resistance of a specific material are used to sense the orientation of the magnetic domains used for encoding the information. In MRI (Magnetic Resonance Image) devices, the interaction between the field and matter allows to distinguish between different tissues and reveal changes caused by pathologies. In controlled nuclear fusion, magnets capable of delivering strong magnetic field are used for the plasma confinement. An example is given by the magnetic field used for the tokamak of ITER (International Thermonuclear Experimental Reactor) that employs a magnetic field of 5.3 T [4]. In the literature, a clear trend toward applications that involve higher magnetic fields is evident. Next-generation particle accelerators will produce a high number of collisions at very high energy, allowing the observation of new or rare phenomena of particle physics. This will be made possible by increasing luminosity and beam energy, the critical performance parameters of an accelerator [5]. Inside the "European strategy for particle physics", significant examples of these technological trends are the High Luminosity Large Hadron Collider (HL-LHC) and the High Energy LHC [6]. For the HL-LHC, stronger superconducting dipole magnets will be installed in the dispersion suppression zone to make space for additional collimators that protect the superconducting magnets [7], [8]. The nominal magnetic field of the dipole magnets will increase from 8.6 T to 11.2 T. New superconducting quadrupole magnets will be installed in the insertion region to increase the focusing properties of the machine, reaching the goal of a much higher luminosity. The nominal field gradient of the new inner triplet quadrupole magnets will change from 200 T/m in an aperture of 70 mm to 132.6 T/m in an aperture of 150 mm [9]. In Fig. 1 the flux density in the cross-section of a 11 T dipole magnet for HL-LHC [10] and of the inner triplet quadrupoles, called MQXF, are shown. In proximity of the coils, the iron yoke shows a level of flux density higher than 3 T. This is due to the higher field generated in the aperture (11 T).

The iron yoke of a superconducting magnet is one of the key elements for its correct operation because it supplies the return path for the magnetic flux and, at the same time, gives mechanical rigidity to the cold mass. Characterizing the magnetic properties of the iron yoke, as well as other materials (i.e. NiFe alloys employed for magnetic shielding) is a necessary task to be carried out in order to predict the behavior of the electromagnetic system to be designed [11]. This is a topic of large interest for the scientific community and a vast literature describing different methods, respectively for different excitation frequency values or various sample shapes [12], [13] and expected behavior, is available [14]–[17]. In the past, low-carbon steel, known under the trade name MAGNETIL BL™ and produced by Cockerill Sambre-

Manuscript received XXXX XX, 2018; revised XXXX XX, 2019. This work was supported by the High-Luminosity Large Hadron Collider (LHC) Project at the European Organization for Nuclear Research (CERN). All the authors equally contributed to this manuscript.

P. Arpaia, and A. Liccardo are with the Department of Electrical Engineering and Information Technology, University of Naples Federico II, Naples, Italy, e-mail: (pasquale.arpaia@unina.it, aliccard@unina.it)

M. Buzio, S.I. Bermudez, and A. Parrella are with the Technology Department, Magnets, Superconductors and Cryostat Group, CERN, European Organization for Nuclear Research, 1211 Geneva, Switzerland, e-mail: (marco.buzio@cern.ch, susana.izquierdo.bermudez@cern.ch, alessandro.parrella@cern.ch)

M. Pentella is with the Department of Applied Science and Technology, Politecnico di Torino, Turin, Italy, with the Department of Electrical Engineering and Information Technology, University of Naples Federico II, Naples, Italy and with the Technology Department, Magnets, Superconductors and Cryostat Group, CERN, European Organization for Nuclear Research, 1211 Geneva, Switzerland, e-mail: (mariano.pentella@cern.ch)

P.M. Ramos is with the Instituto Superior Técnico, Instituto de Telecomunicações, University of Lisbon, Lisbon, Portugal, e-mail: (pedro.m.ramos@tecnico.ulisboa.pt)

E. Stubberud is with the Department of Physics, Norwegian University of Science and Technology (NTNU), Trondheim, Norway and with the Technology Department, Machine Protection and Electrical Integrity Group, CERN, European Organization for Nuclear Research, 1211 Geneva, Switzerland, e-mail: (edvardstubberud@gmail.com)

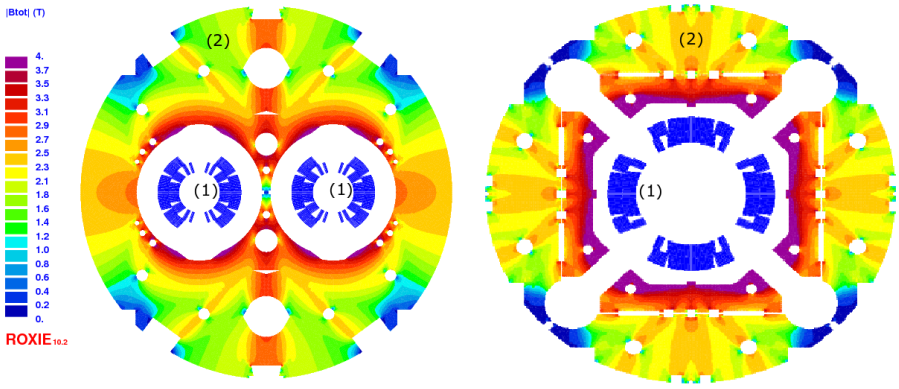

Fig. 1. Flux density in the cross section of MBH 11 T dipoles (left) and in the MQXF quadrupole (right) for HL-LHC. (1) are the windings to create the field in the air gap whereas (2) is the iron yoke.

ARCELOR Group [18], was used for the production of the iron yoke laminations of the LHC main magnets. The magnetic characterization of this material is described in [19], [20]. This would have been the ideal choice also for the new HL-LHC magnets if it had still been available at the moment of the tender. Instead, ARMCO® Pure Iron Grade 4 produced by AK Steel was chosen. An initial magnetic characterization of ARMCO® for fields up to roughly 24 kA/m at room and cryogenic temperatures and different annealing sequences was done in [21] to check the combined effects of annealing, cooling and mechanical strain on the magnetic properties. Nevertheless, considering the increasing level of flux density of the new magnets for HL-LHC, see Fig.1, data at fields up to 3 T in the material are necessary to predict the magnet behavior. This is typically done by using data from compatible materials and assuming that materials with similar purity should have the same behavior in saturation. At low fields, the effect of the yoke can be neglected, since the magnets are coil-dominated [22]. In the past, the problem of the lack of data at high fields was solved by performing measurements on toroidal samples and with a superconducting excitation coil. Kawabata in [23] used this approach for the 10 T single and twin aperture dipoles developed at the National Laboratory for High Energy Physics in Japan (KEK) in collaboration with CERN. Moreover, the iron yoke of the LHC magnets was tested with the same method, reaching a magnetic field up to 2.5 T [19], [20]. These works lack information on the experimental setup. Kawabata [23] did not describe the measurement system design and how the risk of quench was handled. Babic et. al [19], [20] reported only information regarded the number of turns of the superconducting coil. Moreover, experimental data about ARMCO® Pure Iron at fields above 100 kA/m are not available in the literature.

The goals of this paper are mainly two. The former is the design of a superconducting permeameter to characterize magnetic materials at fields up to roughly 500 kA/m, focusing in particular on quench detection and system protection. The latter is to provide data of the magnetic behavior of ARMCO® Pure Iron up to a magnetic field of roughly 3 T.

II. Superconducting permeameter design

A. Experimental method

The experimental method adopted for the tests is the flux-metric method, described in the standard IEC 640404-4 "Magnetic materials - Part 4: Methods of measurement of d.c. magnetic properties of iron and steel" [24] and, in particular, the "point-by-point method" is considered. A sensing coil and an excitation coil are wound around the sample. The excitation coil carries the excitation current to magnetize the sample under test. This current is supplied by a current generator which is controlled by the signal provided by a digital-to-analog converter. The sensing coil detects the induced voltage, that after integration allows the flux to be calculated and, consequently, estimate the magnetic flux density.

The magnetic field $H(r,t)$ is evaluated from the current using

$$H(r,t) = \frac{N_e i(t)}{2\pi r} \tag{1}$$

where N_e is the number of turns in the excitation coil, $i(t)$ is the imposed current and r is the distance from the center of the toroid. H is represented as a scalar for symmetry reasons. The magnetic field is variable within the cross-sectional area of the toroid. Since the difference between external and internal diameter is much lower than the length of the circumference, the magnetic field is assumed constant in the cross-section and equal to its integral average between the inner and the outer radius, $H_0(t)$

$$H_0(t) = \frac{1}{r_2 - r_1}\int_{r_1}^{r_2} H(r,t)dr = N_e i(t)\frac{\ln\frac{r_2}{r_1}}{2\pi(r_2 - r_1)} = \frac{N_e i(t)}{2\pi r_0}. \tag{2}$$

where r_1 is the inner radius of the sample, r_2 is the outer radius of the sample and $r_0 = (r_2 - r_1)/\ln(r_2/r_1)$.

After acquiring the induced voltage on the sensing coil, v, the magnetic flux is determined by integration:

$$\Phi(t) = \int_0^t v(\tau)d\tau \tag{3}$$

The magnetic flux density $B(t)$ is

$$B(t) = \frac{1}{A_s}\left(\frac{\Phi(t)}{N_s} - \mu_0 H_0(t) A_a\right) \tag{4}$$

where N_s is the number of turns of the sensing coil, A_s is the cross-sectional area of the sample and A_a is the cross-sectional area of the air, as represented in Fig. 2.

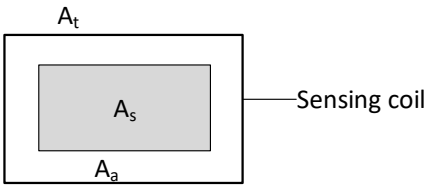

Fig. 2. Representation of the cross-sectional area of the sample A_s and of the sensing coil A_t. The cross-sectional area of the air is $A_a = A_t - A_s$.

The magnetic relative permeability is

$$\mu_r(H) = \frac{B(H)}{\mu_0 H} \tag{5}$$

B. Procedure

The procedure adopted for the tests, consists of three steps: i) demagnetization; ii) magnetization; and iii) post-processing. Firstly, the sample needs to be demagnetized to remove memory-effects from the measurements. Demagnetization is performed by applying an excitation current with a decreasing exponential envelope. Magnetization is performed by ramping the current back and forth between positive and negative values, with the amplitude of each plateau slightly increasing. The ramp rates and the plateau duration are selected so that dynamical effects, predominantly eddy currents, are reduced after a certain percentage of the plateau.

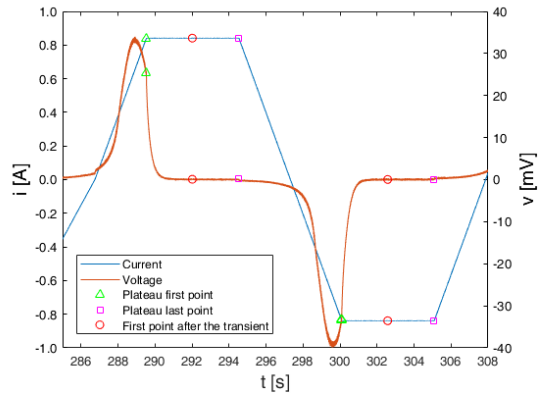

Fig. 3. Normalized excitation current (light blue) and normalized sensing coil voltage curve (red). The triangle, circle and square symbols denote the begin of the plateau, the end of the transient phase and the end of the plateau, respectively.

The waveforms acquired are post-processed by applying the relations from Section II-A, but firstly, it is necessary to correct the voltage acquisition by means of a drift correction algorithm. The acquired voltage $v(t)$ can be expressed as the sum of three contributions

$$v(t) = v_s(t) + v_o(t) + v_n(t) \tag{6}$$

where $v_s(t)$ is the zero-mean induced voltage at the terminals of the sensing coil, $v_n(t)$ is a zero-average random noise and $v_o(t)$ is the offset error, a contribution that depends on various disturbance causes. By integrating $v(t)$

$$\Phi(t) = \int_0^t [v_s(\tau) + v_o(\tau) + v_n(\tau)]d\tau \approx \Phi_s(t) + \Phi_o(t) \tag{7}$$

where $\Phi_s(t)$ is the magnetic flux and $\Phi_o(t)$ is the drift error. The contribution of the random noise is neglected because of the integration operation. In the literature, several drift correction approaches were proposed [25]–[27] The method proposed in this work can be split into the following steps:

1) Identify on each positive and negative plateau, the first and the last point, triangle and square symbols in Fig. 3.
2) Locate the point of the plateau corresponding to the end of the transient due to the ramp-up dynamic effects, circle symbol in Fig. 3.
3) Evaluate for each plateau the offset of the sensing coil signal as the average value of the voltage between the circle and the square symbols in Fig. 3.
4) On the ramps, the offset is estimated by linear interpolation between the offsets of the previous and successive plateau.

Finally, the voltage offset is subtracted to the voltage before the integration. Fig. 4 and Fig. 5 show the estimated voltage offset and its effect on the flux, respectively.

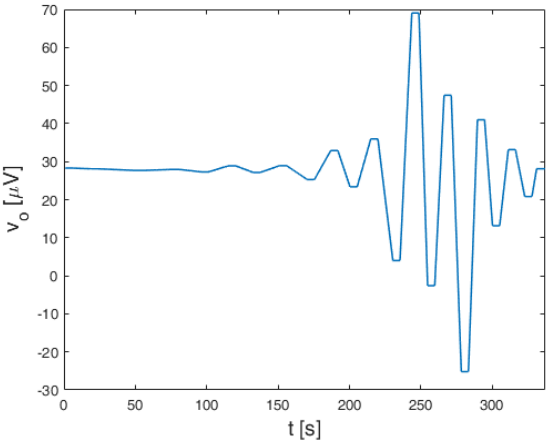

Fig. 4. Example of estimated voltage offset.

The normal magnetization curve is evaluated by taking the points of each hysteresis loop corresponding to the plateau after the transient. The values of the pairs (H, B) are evaluated by averaging the values on the positive and negative plateaus, excluding the points that correspond to the transients.

C. Superconducting permeameter

In Fig. 6, a schematic representation of the superconducting permeameter is shown. It consists in a customized wound

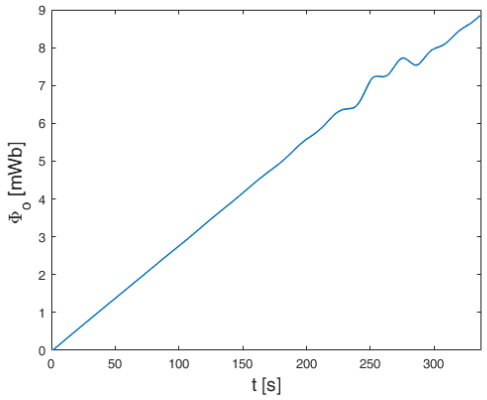

Fig. 5. Flux offset corresponding to the voltage offset of Fig.4.

sample permeameter, prepared according to the standard IEC 60404-4, with in addition some elements allowing to reach roughly 3 T in the material at a temperature of 4.2 K. The ARMCO® sample is inserted in a case of Bluestone to prevent mechanical strain due to thermal shrink. Bluestone was chosen among other alternatives, such as Nylon Glass Fiber, for its very low thermal coefficient (0.01%/K). In order to avoid sharp edges, the case was designed to host a sample with a squared cross-section, but has the corners shaped as in Fig. 6.

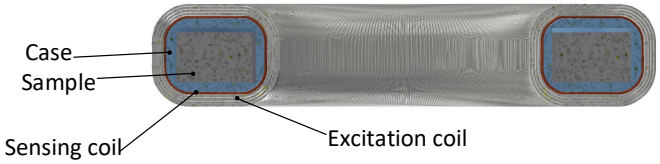

Fig. 6. Sample cross-section view.

Coils are wound directly on the case. The innermost layer is the sensing coil of 90 turns and 0.5 mm in diameter. The excitation coil is made of 4 layers, each one separated from the next using a layer of tape to prevent movement and mechanical disturbances. The cross-sectional diameter of the strand is 0.5 mm without insulation and 0.55 mm with insulation in Polyvinyl Formvar. The strand has a minimum residual-resistivity ratio (RRR) lower than 100 and a matrix in oxygen-free copper with a superconductor-to-copper ratio equal to 2. The four layers of the excitation coil have respectively 566, 484, 459 and 426 turns.

D. Quench simulation and system protection

A quench refers to the sudden loss of superconductivity when the coil temperature is raised. The quench protection analysis aims to assess if the intended currents for the magnet design are safe for operation. This means calculating the hotspot temperature of the magnet during a quench and assessing if the magnet is in need of any form of quench detection. The protection studies consist of three cases, at the operating currents of 40 A, 80 A and 150 A, at a temperature of 4.2 K. The studies consist of several models with different tools.

The first model calculates the magnetic flux density $\boldsymbol{B}$ in the magnet coil and the inductance of the coil in COMSOL, a well-known commercial Finite Element simulator. These values of inductance and magnetic flux density were used to perform the quench simulations. The quench simulations were done by using QLASA, a quench simulation software developed at the LASA laboratories of the INFN [28], [29], coupled with a PSpice circuit. The COMSOL model is an axisymmetric 2D model of the toroidal coil cross-section. In the model, the cross-section of the iron sample and the Bluestone case around the sample have the same dimensions as the real torus and case, whereas the shape of the coil is simplified. The new coil consists of a single conductor with the same current density as each winding in the original coil. The thickness of this simplified conductor scales proportional to the inverse of the radius of the torus, see Fig. 7. This scaling compensates for the fact that the winding density reduces with the radius of the torus.

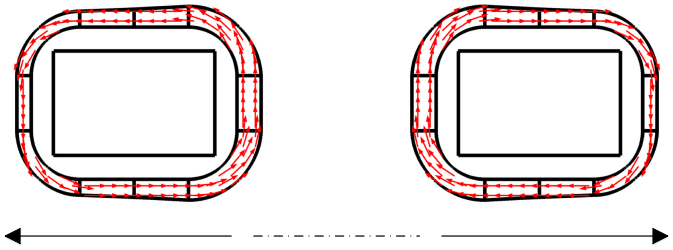

Fig. 7. Current distribution used in the simulations.

From the COMSOL model, the magnetic flux density in two given points of the coil (P_1 and P_2) were extracted, see Fig. 8. The points are located inside and outside of the coil, at the smallest radius of the torus. In correspondence of these points, the maximum value of the magnetic flux density is estimated. To calculate the inductance, COMSOL uses the two equations for magnetic energy $U = \frac{1}{2}LI^2$ and $U = \frac{1}{2}\int_\Omega B \cdot H d\Omega$, which yield

$$L = \frac{1}{2I^2}\int_\Omega B \cdot H d\Omega. \tag{8}$$

In absence of real data concerning the ARMCO® *B-H* curve, for these simulations a set of data from the LHC magnets was used.
The values calculated by COMSOL are shown in Table I.

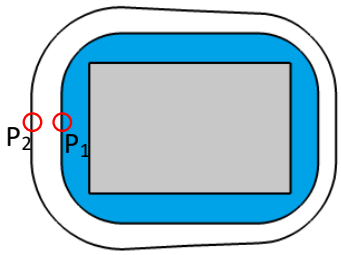

Fig. 8. Cross-section of the toroidal coil with the two points, P_1 and P_2.

TABLE I
VALUES OF THE MAGNETIC FLUX DENSITY AND INDUCTANCE FOR CURRENT VALUE.

Current I	Inductance L	$B(P_1)$	$B(P_2)$
40 A	0.04592 H	0.0040 T	0.5733 T
80 A	0.02971 H	0.0080 T	1.1466 T
150 A	0.02213 H	0.0149 T	2.1500 T

Since QLASA is an analytic 3D tool to calculate the quench behavior of superconducting solenoids, some assumptions were made to transform the toroidal geometry into a solenoid. The toroidal coil was transformed into a solenoid by assuming constant cross-section and volume of the coil. The cross-section winding area of the solenoid was approximated by the area of the innermost cross-section of the windings in the r-θ-plane of the toroid. The length of the solenoid was approximated to the innermost circumference of the torus with windings. The QLASA model assumes the magnetic field around the solenoid to be symmetric to the center of the solenoid. This is not the case for the toroidal coil, where the field varies with the radius of the torus. To achieve conservative results in the simulations, the peak values of the magnetic flux density at the inside and outside of the solenoid was respectively set to P_1 and P_2. The magnetic flux density was assumed constant along the length of the solenoid. The QLASA simulations are based on adiabatic conditions, which implies no heat transfer to the surrounding helium. Assuming adiabatic conditions for the toroidal coil was reasonable since the coil wires are isolated from the helium bath, and the heating of the coil due to a quench happens in a time interval on the scale of 100 ms. PSpice is another well-know commercial software used to simulate a circuit with the same properties as in the experimental setup. The circuit setup was simulated by adopting a current generator in parallel with the diode, represented using a switch in series with a resistance R_D equal to 1 mΩ, and the toroidal coil was represented using an inductance in series with variable resistance. At nominal operation, the crowbar is open, and the power converter supplies a constant current through the coil, as shown in Fig. 9. The crowbar is open, and the current flows through the load, with $r(t)$ equals to zero. During a superconductor quench, the resistance $r(t)$ in the coil grows, and consequently the coil voltage increases. Once the voltage over the coil reaches a certain threshold, the power converter turns off, and the crowbar closes.

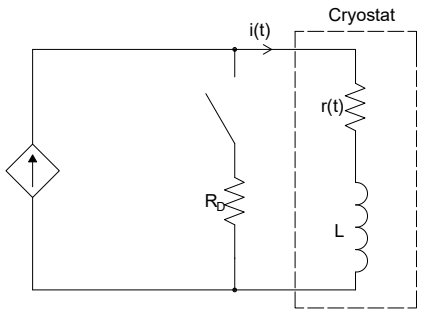

Fig. 9. Electrical Circuit used for the quench protection simulations.

The voltage threshold over the coil was set to 1 V. The results for a current of 40, 80 and 150 A are shown in Fig. 10. From the results, the hotspot temperature rises to a maximum value of 30.4 K for 40 A, 46.5 K for 80 A and 69.7 K for 150 A, i.e., well below 100 K at which the increase in thermal expansion coefficient may result in increased stress. The results show that the toroidal coil is self-protected in all the study cases. The threshold voltage of the power controller governs the limit of the ramp rate in the coil. The average max ramp rate is calculated from $(dI/dt)_{max} = V_t/L$, where V_t is the threshold voltage and L is the inductance reported in Table I. With the threshold voltage set to 1 V, the average max ramp rate is 21.7 A/s for 40 A, 33.7 A/s for 80 A and 44.2 A/s for 150 A.

E. Measurement system layout

The system architecture is shown in Fig. 11. The digital acquisition system consists of a 16 slot PXI crate which contains an NI DAQ 4462, a 24 bit board with two analog acquisition channels (AI) and two analog output channels (AO). The AIs are used to acquire the current, and the induced voltage and one AO is used to command the voltage-controlled power supply. The current is sensed with a current transducer (DCCT) MACC$^{\text{PLUS}}$ 2 of 120 A. A NI DAQ M-6289 is used to command a switch in parallel with the system. The initial instabilities of the NI 4462 AO could bring to undesired current variations in the excitation coil, that could affect the measurement itself. To avoid this, the power supply is connected to the permeameter only after a delay of about 50 ms.

Two power diodes with a nominal current of 90 A and 600 V of nominal voltage are placed in anti-parallel for the system protection. Finally, an interlock panel reads the state of the circuit breaker and, if this is open, it blocks the power supply.

III. RESULTS AND DISCUSSION

A. Magnetic properties of ARMCO®

Fig. 12 shows the initial magnetization (left) and the relative permeability (right) curves of the material. The initial magnetization curve was measured up to a magnetic flux density of 2.82 T, corresponding to a magnetic field of about 450 kA/m. For such a level of the magnetic field, the relative permeability is 5. The permeability peak value of 1750 appears at a magnetic field of about 350 A/m. The measurements have a relative expanded uncertainty of 0.01% (with a coverage factor of 2) on the values of H and uncertainty of 1% on the values of B and μ_r. In Fig. 12a, the red curve corresponds to the initial magnetization curve calculated using the Wlodarski [30].

$$M(H) = M_a \mathcal{L}\left(\frac{H}{a}\right) + M_b \tanh\left(\frac{|H|}{b}\right)\mathcal{L}\left(\frac{H}{b}\right) \quad (9)$$

where $\mathcal{L}$ is the Langevin function, $M_a + M_b$ represents the saturation magnetization, a and b the rate of approach to the saturation.

The parameters of the equation, retrieved by using the method described by Wlodarski in [30], are: $\mu_0 M_a$=0.49224 T,

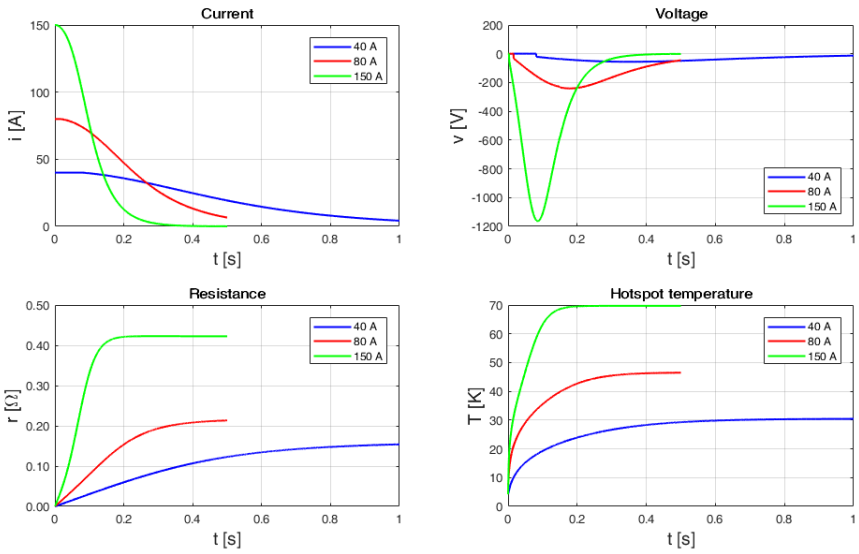

Fig. 10. Current decay and hotspot temperature for three case studies.

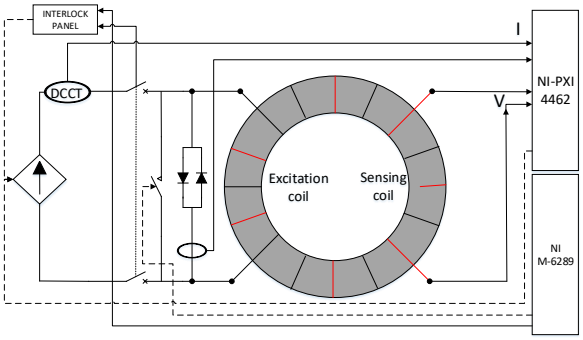

Fig. 11. Setup of the measurement system, showing how all the components are connected.

$\mu_0 M_b$ =1.7478 T, a =9340.0 A/m and b =214.59 A/m. The Wlodarski fitting shows higher values of flux density at low fields (up to 200 A/m). This because the fitting does not take into account some physical phenomena that occur in this region. In particular, with this set of parameters, there is a maximum difference of 0.15 T at 160 A/m whereas an average difference of roughly 12 mT occurs at higher fields. Fig. 13 shows a comparison between the initial magnetization curve of i) ARMCO® (data presented in this work), ii) MAGNETIL (data from LHC magnets' production), and iii) a standard steel (data from ROXIE database). The three *B-H* curves show a very similar magnetic behavior when well saturated ($H > 3000$ A/m). This means that the three materials have a similar chemical composition. Nevertheless, for $H < 3000$ A/m ARMCO® shows a completely different behavior, while the other two present similar shapes. This means that these last two were annealed or cold worked differently. The region of interest for the new superconducting magnets for HL-LHC is also shown in Fig.13. Although the three materials seem to have the same magnetic behavior (same shape of the B-H curve), in the region $20000 < H < 100000$ A/m MAGNETIL and ARMCO® present a higher flux density values than ROXIE material, while for $H > 100000$ A/m, ARMCO® shows higher flux density values than MAGNETIL that shows higher flux density values than ROXIE material. This demonstrates the importance of characterizing materials for magnet yokes at their operating magnetic field. This comparison also raises the problem of checking how big is the impact of using a wrong *B-H* curve during the magnet design phase. This problem is addressed in the following section for the new HL-LHC superconducting quadrupoles and dipoles.

B. Impact of the BH on the field quality

This section evaluates the impact of the iron magnetic properties on the magnetic transfer function (TF), defined as the ratio between the main field and the magnet current. The two Nb_3Sn High Field Superconducting magnets for the HL-LHC, MQXF and the MBH-11T are studied. Simulations are performed in ROXIE, a BEM-FEM 331 program developed at CERN [31], using three different *B-H* curves: i) ROXIE database, ii) MAGNETIL measurements reported in [19], [20], iii) ARMCO® measurements reported in this paper. MBH-11T is 60 mm aperture dipole and 11.2 T field, operating at a nominal current of 11.85 kA. Each coil consists of 56 turns, 22 in the inner layer and 34 in the outer layer. The magnetic length is 5.3 m, meaning that two 11 T magnets are delivering the same integrated magnetic strength as one 8.3 T LHC main bending dipole. The transfer function on the magnet cross section as a function of the current is shown in Fig. 14 (right). The different iron magnetization behavior has a significant impact on the main field. The transfer function at the nominal field is 4.5 mT/kA higher in the case of ARMCO® as compared to ROXIE database and 2 mT/kA higher for MAGNETIL, showing the importance of a good

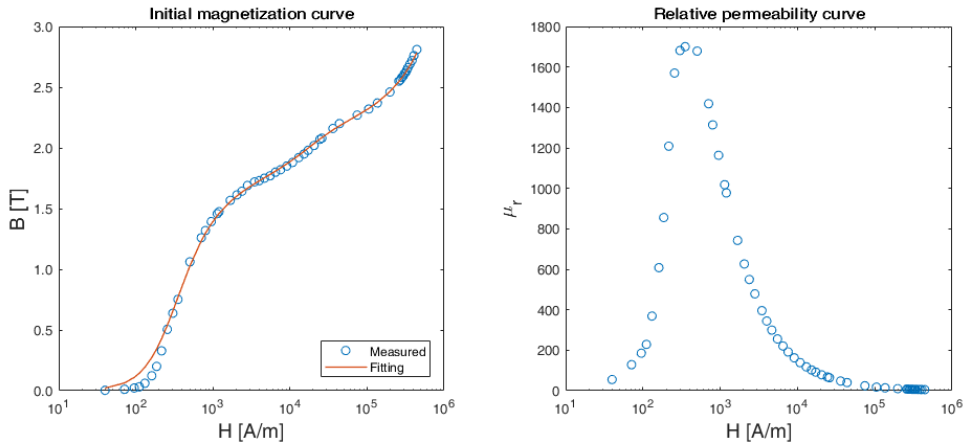

Fig. 12. Measurement results of the characterization up to a magnetic flux density of 2.82 T. The curve in red is the fitting obtained by using the Wlodarski's equation.

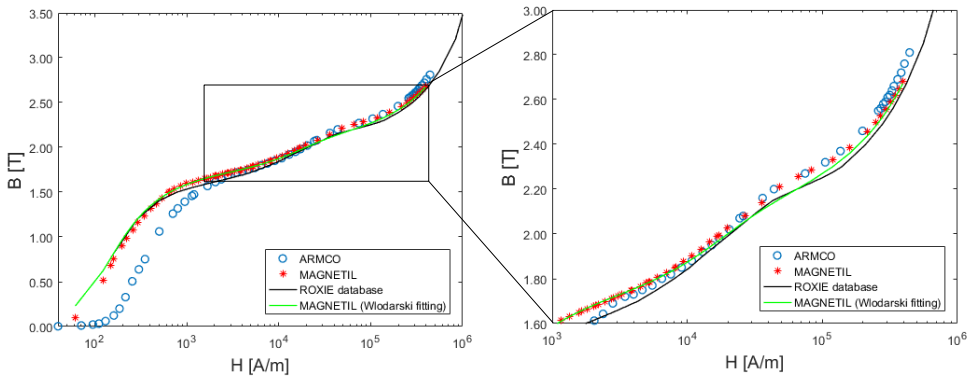

Fig. 13. Comparison between the initial magnetization curve of i) ARMCO® (data presented in this work), ii) MAGNETIL (data from LHC magnets' production), and iii) a standard steel (data from ROXIE database).

magnetic characterization of the iron yoke (0.2% and 0.4% compared to the curve evaluated by using ARMCO®). MQXF is a 150 mm diameter aperture quadrupole and 132.6 T/m gradient, operating at a nominal current of 16.46 kA. Each coil consists of 50 turns, 22 in the inner layer and 28 in the outer layer. The magnet will be produced in two lengths, MQXFA and MQXFB, with a magnetic length of 4.2 m and 7.15 m respectively. Fig 15, left, shows the transfer function in the magnet straight section as a function of the current. The TF decreases by around 9 % from injection to nominal current due to the iron saturation effect. For this case, the different iron magnetization behavior has an even more significant impact on the main field. The transfer function at nominal field varies in the worst case of roughly the 0.8%.

IV. Conclusion

In this paper, the problem of characterizing magnetic properties of the new HL-LHC magnet yokes at the operating temperature and saturation level was addressed. The solution consisted of a measurement system, called superconducting permeameter, based on a flux-metric method. The main problem of employing superconducting coils, an undesired quench, was addressed successfully by specific quench protection simulations, which lead to a self-protected system. The magnetic characterization of the material for the new HL-LHC superconducting magnet yokes was performed at the cryogenic temperature of 4.2 K. From these, the values at 1.94 K, the operating temperature of the LHC magnets, can be easily obtained. The results present an initial magnetization and relative permeability curves up to nearly 450 kA/m, the higher value of saturation being 2.82 T. Similar levels of saturation are expected when the magnets will be powered at their nominal current values. The properties of this material were compared with the material used for the LHC magnet yokes and with similar material from ROXIE database. Significant discrepancies were found, especially at higher levels of saturation. The common assumption that heavily-saturated steels with similar chemical composition behave precisely the same way was proofed wrong. Finally, two case studies based on the new HL-LHC superconducting magnets were presented. Whereas the dipole magnets are less affected, the quadrupoles transfer function shows a significant dependency on the magnet yoke properties. Hence, the characterization of the employed material at its operating temperature and magnetic saturation

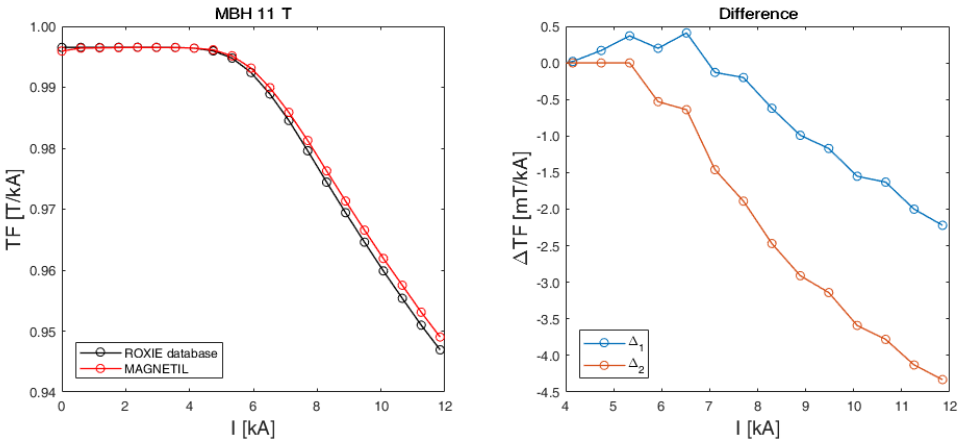

Fig. 14. Comparison between the MBH-11 T transfer functions based on the BH curves of Fig.13. Δ_1 and Δ_2 are the difference between the transfer function evaluated by using the actual curve of the material and the transfer functions evaluated, respectively, by using the ROXIE curve and the MAGNETIL curve.

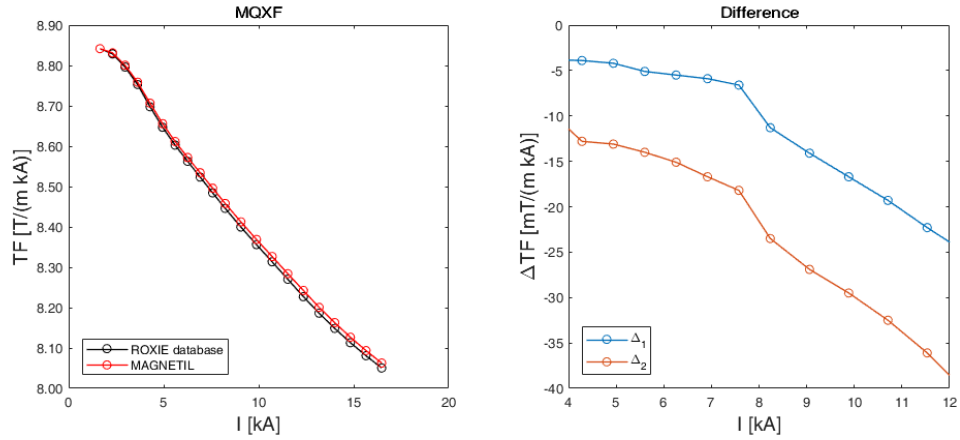

Fig. 15. Comparison between the MQXF transfer functions based on the BH curves of Fig.13.

level is necessary for such a level of field intensity.

ACKNOWLEDGMENT

The authors thank G. Kirby and S. Russenschuck for the useful discussion about applied superconductivity. R. Principe for its cooperation and the provision of the samples. M. Mentink and L. Bortot for the help with quench simulations. R. B. Mercadillo, T. Koettig and S. Prunet for the technical support to the cryogenic permeability measurements.

REFERENCES

[1] M. Hall, O. Thomas, H. Smith, and P. Anderson, "Equivalence of measurements on soft magnetic materials in the UK and measurements for operational conditions," *IEEE Transactions on Instrumentation and Measurement*, vol. 60, no. 7, pp. 2275–2279, 2011.

[2] Y. Ege, M. G. Sensoy, O. Kalender, and S. Nazlibilek, "Numerical analysis for remote identification of materials with magnetic characteristics," *IEEE Transactions on Instrumentation and Measurement*, vol. 60, no. 9, pp. 3140–3152, 2011.

[3] E. Putilova, E. Gorkunov, S. Zadvorkin, and L. Goruleva, "The applicability of magnetic method to the estimation of the current state of laminated steel materials and their separate components by magnetic parameters," in *AIP Conference Proceedings*, vol. 1785, no. 1. AIP Publishing, 2016, pp. 040 052–1–4.

[4] P. Lamalle, B. Beaumont, F. Kazarian, T. Gassmann, G. Agarici, P. Ajesh, T. Alonzo, B. Arambhadiya, A. Argouarch, R. Bamber *et al.*, "Status of the ITER Ion Cyclotron H&CD system," *Fusion Engineering and Design*, vol. 88, no. 6-8, pp. 517–520, 2013.

[5] L. Rossi, O. Brüning *et al.*, "High luminosity large hadron collider," in *European Strategy Preparatory Group-Open Symposium, Krakow*, 2012.

[6] M. Krammer, "The update of the European strategy for particle physics," *Physica Scripta*, vol. 2013, no. T158, pp. 014 019–1–7, 2013.

[7] E. Todesco, H. Allain, G. Ambrosio, G. Arduini, F. Cerutti, R. De Maria, L. Esposito, S. Fartoukh, P. Ferracin, H. Felice *et al.*, "A first baseline for the magnets in the high luminosity LHC insertion regions," *IEEE Transactions on Applied Superconductivity*, vol. 24, no. 3, pp. 1–5, 2014.

[8] G. Ambrosio, "Nb3Sn high field magnets for the high luminosity LHC upgrade project," *IEEE Transactions on Applied Superconductivity*, vol. 25, no. 3, pp. 1–7, 2015.

[9] L. Bottura, G. de Rijk, L. Rossi, and E. Todesco, "Advanced accelerator magnets for upgrading the LHC," *IEEE Transactions on Applied Superconductivity*, vol. 22, no. 3, pp. 4 002 008–1–8, 2012.

[10] F. Savary, E. Barzi, B. Bordini, L. Bottura, G. Chlachidze, D. Ramos, S. I. Bermudez, M. Karppinen, F. Lackner, C. Löffler *et al.*, "The 11 T dipole for HL-LHC: Status and plan," *IEEE Transactions on Applied Superconductivity*, vol. 26, no. 4, pp. 1–5, 2016.

[11] J. R. Anglada, P. Arpaia, M. Buzio, A. Liccardo, A. Parrella, M. Pentella, and P. M. Ramos, "On the importance of magnetic material characterization for the design of particle accelerator magnets," in *Journal of Physics: Conference Series*, vol. 1065, no. 5. IOP Publishing, 2018, pp. 052 045–1–4.

[12] F. Fiorillo, "Measurements of magnetic materials," *Metrologia*, vol. 47, no. 2, p. S114, 2010.

[13] Z. Gmyrek, "Single sheet tester with variable dimensions," *IEEE Trans-*

actions On Instrumentation And Measurement, vol. 65, no. 7, pp. 1661–1668, 2016.

[14] B. Tellini, M. Bologna, and A. Petri, "Measurement of magnetism in composite materials," *IEEE Transactions on Instrumentation and Measurement*, vol. 58, no. 10, pp. 3411–3417, 2009.

[15] B. Tellini, R. Giannetti, and S. Lizon-Martinez, "Sensorless measurement technique for characterization of magnetic material under nonperiodic conditions," *IEEE Transactions on Instrumentation and Measurement*, vol. 57, no. 7, pp. 1465–1469, 2008.

[16] B. Tellini, R. Giannetti, S. Lizon-Martinez, and M. Marracci, "Characterization of the accommodation effect in soft hysteretic materials via sensorless measurement technique," *IEEE Transactions on Instrumentation and Measurement*, vol. 58, no. 8, pp. 2807–2814, 2009.

[17] S. Di Fraia, M. Marracci, B. Tellini, and C. Zappacosta, "Shielding effectiveness measurements for ferromagnetic shields," *IEEE Transactions on Instrumentation and Measurement*, vol. 58, no. 1, pp. 115–121, 2008.

[18] P. Harlet, F. Beco, and L. Renard, "Process for manufacturing mild steel ," 7 1994, patent EP 0681031A1-B1. [Online]. Available: https://patents.google.com/patent/EP0681031A1/en?oq=EP+0681031

[19] S. Babic, S. Comel, F. Beckers, F. Brixhe, G. Peiro, and T. Verbeeck, "Toward the production of 50 000 tonnes of low-carbon steel sheet for the LHC superconducting dipole and quadrupole magnets," *IEEE Transactions on Applied Superconductivity*, vol. 12, no. 1, pp. 1219–1222, Mar 2002.

[20] F. Bertinelli, S. Comel, P. Harlet, G. Peiro, A. Russo, and A. Taquet, "Production of Low-Carbon Magnetic Steel for the LHC Superconducting Dipole and Quadrupole Magnets," *IEEE Transactions on Applied Superconductivity*, vol. 16, no. 2, pp. 1777–1781, June 2006.

[21] A. Parrella, P. Arpaia, M. Buzio, A. Liccardo, M. Pentella, R. Principe, and P. M. Ramos, "Magnetic Properties of Pure Iron for the Upgrade of the LHC Superconducting Dipole and Quadrupole Magnets," *IEEE Transactions on Magnetics*, pp. 1–4, 2018.

[22] S. Russenschuck, *Field computation for accelerator magnets: analytical and numerical methods for electromagnetic design and optimization*. John Wiley & Sons, 2011.

[23] S. Kawabata, "Magnetic permeability of the iron yoke in high field superconducting magnets," *Nuclear Instruments and Methods in Physics Research Section A: Accelerators, Spectrometers, Detectors and Associated Equipment*, vol. 329, no. 1-2, pp. 1–8, 1993.

[24] IEC, "Magnetic materials-part 4: Methods of measurement of dc magnetic properties of magnetically soft materials," 2000.

[25] J. García and M. Rivas, "A quasi-static magnetic hysteresis loop measurement system with drift correction," *IEEE transactions on magnetics*, vol. 42, no. 1, pp. 15–17, 2006.

[26] C. G. C. Carducci, M. Marracci, F. Attivissimo, R. Giannetti, and B. Tellini, "An Improved DAQ-Based Method for Ferrite Characterization," *IEEE Transactions on Instrumentation and Measurement*, vol. 66, no. 9, pp. 2413–2421, 2017.

[27] C. G. C. Carducci, A. Di Nisio, F. Attivissimo, and A. Trotta, "Dynamic error correction for magnetic property measurement," *IEEE Transactions on Instrumentation and Measurement*, 2019.

[28] L. Rossi and M. Sorbi, "QLASA: A computer code for quench simulation in adiabatic multicoil superconducting windings," *Nat. Inst. of Nucl. Phys.(INFN), Rome, Italy, Tech. Rep. TC-04-13*, 2004.

[29] G. Manfreda, L. Rossi, and M. Sorbi, "MATPRO upgraded version 2012: a computer library of material property at cryogenic temperature," *Tech. Rep. INFN-12-04/MI*, 2012.

[30] Z. Włodarski, "Analytical description of magnetization curves," *Physica B: Condensed Matter*, vol. 373, no. 2, pp. 323–327, 2006.

[31] S. Russenschuck, "ROXIE: the Routine for the Optimization of Magnet X-sections, Inverse Field Computation and Coil End Design," CERN, Tech. Rep., 1993.